A morphological and chemical classification of bronze corrosion features from an Iron Age hoard (Tintignac, France): the effect of metallurgical factors

ACTA IMEKO
ISSN: 2221-870X
December 2022, Volume 11, Number 4, 1 - 10

A morphological and chemical classification of bronze corrosion features from an Iron Age hoard (Tintignac, France): the effect of metallurgical factors

Giorgia Ghiara[1], Christophe Maniquet[2], Maria Maddalena Carnasciali[1], Paolo Piccardo[1]

[1] *Department of Chemistry and Industrial Chemistry (DCCI), University of Genoa, Via Dodecaneso 31, 16146 Genova, Italy*
[2] *INRAP Limoges, 18 allée des Gravelles, 87280 Limoges, France*

ABSTRACT
A categorization of corrosion morphologies of archaeological Sn bronzes was carried out on archaeological Iron Age objects. The objects come from a Celtic deposit located in central France (Tintignac, Corrèze) and are dated between 2nd and 3rd cent BC. Being samples of corroded metals taken from a single find spot, parameters connected to the features of the alloy and known to influence the corrosion morphologies were thoroughly considered. Global processes were highlighted, and corrosion mechanisms were characterised with a multi-analytical protocol (SEM-EDS, micro-Raman spectroscopy, image analyses) according to the detected morphology. Elaboration of the results was carried out with a multicomponent approach. Results show the presence of 5 different morphologies correlated to the alloys characteristics of the objects. Alloy composition, microstructure, degree of deformation and grain size were found to influence the corrosion products formed and the morphology of the attack. In particular, the 'tentacle like corrosion', associated to a microbial attack was the most susceptible to the effect of metallurgical features: their occurrence is connected to a more massive presence of Fe and Pb in the alloy, a homogeneous deformation and a larger grain size.

Section: RESEARCH PAPER

Keywords: Corrosion morphology; Sn bronze; microstructure; tentacle like corrosion; MIC

Citation: Giorgia Ghiara, Christophe Maniquet, Maria Maddalena Carnasciali, Paolo Piccardo, A morphological and chemical classification of bronze corrosion features from an Iron Age hoard (Tintignac, France): the effect of metallurgical factors, Acta IMEKO, vol. 11, no. 4, article 11, December 2022, identifier: IMEKO-ACTA-11 (2022)-04-11

Section Editor: Tatjana Tomic, Industrija nafte Zagreb, Croatia

Received April 14, 2022; **In final form** July 14, 2022; **Published** December 2022

Corresponding author: Giorgia Ghiara, e-mail: giorgia.ghiara@gmail.com

1. INTRODUCTION

Archaeological objects constitute our main source of information to study the corrosion behaviour of copper-based alloys over long timespans. Ancient metals buried in soil or left in waterlogged environments for centuries give the most reliable data on how to model and thus predict the corrosion behaviour of modern alloys [1]-[4]. When studying the overall corrosion process, it is straightforward that the environment itself must be considered. Much research already studied the variety of environments and features occurring [5]-[10] on Sn-bronzes, pointing out the importance of water (the electrolyte in the corrosion process) and the nature and concentration of dissolved salts inside the solution. The morphology, composition, physical and chemical features of the corroded layer derive from the interaction with these corrosive agents [11]-[13]. The rate and morphology of the attack is thus affected by i) the anodic or cathodic processes that promote the growth of salts or the formation of complexing ions; ii) the evolution of the moving equilibria in the anodic or cathodic direction; ii) the conductivity of the solution [14], [15]. Corrosion of soil can be more challenging since, other than water, climatic parameters as rainfall, wind, sunlight, temperature, and microbiological activity influence the composition and the properties of the system and allow for different types or mechanisms to occur, one after the other or even simultaneously [16].

Nevertheless, the environment is not the only parameter that scientists must consider when dealing with corrosion processes of Sn-bronzes. The composition and the microstructural features of the matrix are prominent if the alloys are exposed to the same environmental conditions. Focusing on the composition, corrosion properties as nobility, passivity or cathodic and anodic processes are related to the influence of the alloying elements and

their quantity inside the matrix [14]-[16]. From a historical point of view typical alloying elements are As, Zn and Sn, the latter providing the better corrosion resistance [17]-[20]. Furthermore, the quantity of the alloying element inside the solid solution can be beneficial or detrimental to the corrosion resistance of the material. Research on the performances of single-phase Cu-Sn alloys and how the growth of a passive film on the surface is promoted by large supplementations of Sn to pure Cu [17]-[19] were undertaken in the past. Also, how a high Zn content in brasses promotes a dezincification mechanism is a common phenomenon [20]. However, corrosion can be triggered also according to metallurgical features as heterogeneities, impurities, secondary phases, defects, or grain orientation [14]. The presence of impurities or defects can cause higher corrosion rates by creating preferential areas of corrosion [16] as heterogeneities inside the solid solution or intermetallic phases can lead to a selective type of corrosion. The presence of detrimental secondary phases was also described in recent studies [21].

Generally, the action of each parameter is reflected in a specific corrosion morphology that is categorized accordingly [7], [10], [22]-[26]. Various corrosion morphologies are presented in literature and are generally correlated to the work of Robbiola et al. [7]. In their work, the authors defined two types of corrosion features for archaeological Tin-bronzes in soil, according to the preservation of the original surface that allows to define the original shape of the artefact. These models were obtained on a statistical study of Sn-bronzes with a Sn range of composition from 4 to 23 wt. % and coming from the same site of excavation. Both corrosion morphologies derive from an electrochemical process of oxidation of the metal (anode) and reduction of the oxygen (cathode). After the buildup of a corrosion layer, the mechanism described further developed with the mobility of cationic and anionic species, that interact with each other within the metal-soil system [7]. However, the influence of metallographic features was less considered and typical metallurgical parameters as alloy composition, microstructure, fabrication and/or finishing techniques were not considered.

The study wants to fill the gap on archaeological materials by considering the metallurgical parameters to play an important role in the corrosion mechanism of artifacts buried in soil. The archaeological objects come from a recently excavated deposit (Tintignac, Corrèze) located in the central part of France, from which it was possible to obtain the necessary information to properly interpret the corrosion behavior without external contaminations.

2. MATERIALS AND METHODS

2.1. Archaeological context

A Celtic deposit was discovered around Tintignac (Naves, Department of Corrèze) in the southwest of central France and dated between 2nd and 3rd cent BC (Figure 1).

Different bronze and iron objects related to warfare were deposited in a pit in the north-western area of a ritual or cultic place (fanum). Most of the objects were intentionally destroyed before the deposition. The square pit measured around 1 m^2 and 30 cm depth and around 60 metallic objects were discovered: defensive armour (shields and helmets), war trumpets (*karnykes*), and a wide variety of other artifacts. To minimize the number of variables in the study, binary bronzes with no secondary phases are taken into consideration and only composition and microstructural features are analysed.

2.2. Methodology

Small size fragments suitable for metallurgical investigations were sampled. Of each fragment/object, one or more (1 to 3) samples were taken. After a preliminary visual observation to verify the surface characteristics and preservation, samples were mounted in cold resin and subsequently polished with decreasing grain-size diamond suspensions up to 1 μm, in agreement with the ASTM E3-01 standard procedure. The protocol was designed to characterise the objects through metallurgical investigations of the metallic matrix and spectroscopic analyses of the corrosion layers. Objects were studied and categorized according to the morphology, composition, and microstructural features.

2.3. Analytical techniques

A preliminary characterisation was performed prior to metallographic etching by light optical microscopy (LOM; MEF4 M; Leica Microsystems, Buffalo Grove, IL, USA) using bright-field (BF) and dark-field (DF) contrast methods. The latter is particularly suitable for detecting corrosion products and allows for an exhaustive detection of the mineralized areas [27]. The microstructural features of the metallic matrix and the morphology of the corrosion process were documented by LOM and Scanning Electron Microscopy (SEM; Zeiss Evo40; Carl Zeiss, Oberkochen, Germany). Chemical analyses of the metallic substrate and the corroded layers were performed with energy-dispersion X-ray spectroscopy (EDXS; Cambridge INCA 300 with PentaFET EDXS detector (Oxford Instruments, Oxfordshire, U.K.) sensitive to light elements, Z> 5) connected to the SEM. The EDS was previously calibrated on a cobalt

Figure 1. Different layers of the Celtic deposit discovered around Tintignac (Naves, Department of Corrèze, France) and dated between 2nd and 3rd cent BC. (a) upper level, (b) middle level; (c) lower level.

standard. This procedure allowed to obtain reliable values for all elements with atomic weight higher than 11 ($Z \geq 11$), while for lighter elements like oxygen the analysis was considered as semi-quantitative. Amounts below 0.2 wt.% were considered as semi-quantitative measurements and were evaluated only when the identification peaks were clearly visible in the acquisition spectrum. The reported compositions of the alloys correspond to the average of at least five measurements on non-corroded areas. All results on the alloys were normalized and presented in average weight percent. Afterwards, chemical etching was performed on the samples with a solution of $FeCl_3$ (5 g) diluted in HCl (50 mL) and ethanol (200 mL) to reveal their microstructural features. To estimate the grain size, the procedure using the grain boundary intersection count was carried out according to the ASTM E-112 standard. The degree of deformation of the alloy was calculated following equations from [28], [29]. The shape factor of the inclusions (sf) can be computed by calculating their width/length ratio and by correlating it to the stress absorbed by the material. The deformation applied, resulting in a reduction of thickness (D%), is described as:

$$D\% = \frac{thick_0 - thick_{\text{end}}}{thick_0} \cdot 100\ \%\,, \tag{1}$$

where $thick_0$ and $thick_{\text{end}}$ are the initial and final thickness respectively. The equation was then further implemented correlating the sf of the inclusions to the deformation applied:

$$D\% = \frac{sf - \sqrt[3]{sf}}{sf} \cdot 100\ \%\,, \tag{2}$$

$$thick_0 = thick_{\text{end}} \cdot sf^{\frac{2}{3}}\,. \tag{3}$$

To determine the nature of the corrosion products, micro-Raman spectroscopy (μRS, Renishaw Raman System 2000, Renishaw, Inc., Hoffman Estates, IL, USA) was also employed. The instrument was supplied with a charge coupled device (CCD) Peltier-cooled as detector and excited using a 632.8 nm He-Ne laser at 1 cm-1. To estimate the thickness of the corroded layers and the percentage of sound metal on the sample an image analysis software (Fiji-ImageJ, version 1.49b) was used on 100 x LOM micrographs [30].

A statistical procedure was also performed using the Principal Component Analysis (PCA) to evidence correlations between the variables and possible clustering of the samples. The original data matrix was decomposed into two smaller matrices: the loadings, which can be interpreted as the weights for each original variable in the PC computation, and the scores, which contain the original data in the newly rotated coordinate system [31]. Also, a biplot was created with both the loadings (variables) and scores (samples) positions on the new coordinate system.

3. RESULTS AND DISCUSSION

3.1. Metallurgical Characterisation

All objects are made of Sn-bronze with Sn as the major alloying element and minor elements as As, Ni, Co, Fe and Pb. Figure 2 describes the number of objects and the frequency distribution according to the element considered (Sn, Fe, As, Pb, Ni, Co).

Sn disperses from 6 % to 16 % in wt., with the highest occurrence (more than the 80 % of the samples) found for the interval 10 – 14 % in wt. confirming the high technological skills

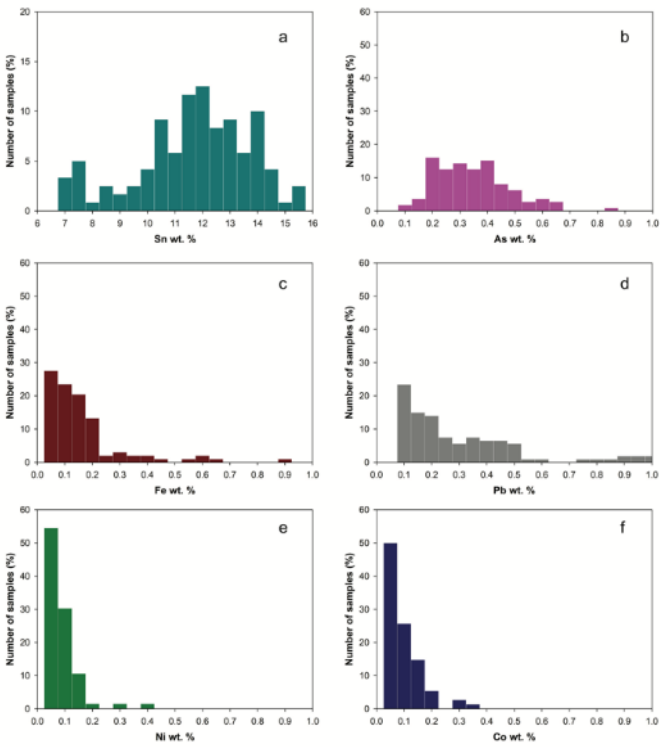

Figure 2. Frequency distribution of major and minor alloying elements detected on the whole number of samples: (a) Sn; (b) As; (c) Fe; (d) Pb; (e) Ni; (f) Co.

of the Celtic culture [32]. Minor elements as As, Ni, Co, Fe and Pb concentrations are below 1 wt.% (even less than 0.2 wt. %), with variations of the shape of the curve according to the element. Fe, Pb, Co and Ni are show very high frequency in the range below 0.2 wt. %, which is close to the limit of detection (LOD) of the EDS. This outcome should be considered as semiquantitative, and more sensitive analytical techniques are needed to confirm the distribution curve proposed in this study. The element As showed on the other hand experimental values modelled with a gaussian-like curve, with a distribution probability centred at 0.3 wt. %. A microstructural investigation was performed through LOM and SEM investigations, and Figure 3 displays the features observed. They are characterised

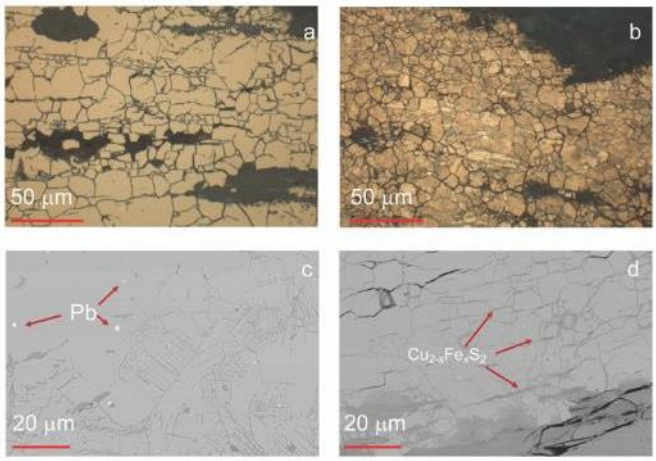

Figure 3. Microstructures observed on the objects. LOM micrographs of: (a) polygonal grains typical of recrystallization annealing; (b) twinning and slip lines; SEM-BSE micrographs highlighting the composition of inclusions: (c) Pb; (d) $Cu_{2-x}Fe_xS_2$.

Table 1. Description of the corrosion morphologies identified in the study.

Corrosion Morphology	Description	Penetration	Corrosion products
Type A	So called classical archaeological bronzes corrosion mechanism in presence of water. Intergranular corrosion. Red, yellowish-orange, green and blue are the predominant colors	Short-circuit of diffusion: e.g., grain boundaries, slip bands, mechanical twins. Interdiffusion of ions from both the metallic substrate (Cu, Pb, As, Ni, Fe) and the soil (Si, Al, Fe)	Cuprite (Cu_2O); Cassiterite (SnO_2); Malachite ($Cu_2CO_3(OH)_2$); Azurite ($Cu_3(CO_3)_2(OH)_2$; mixed forms of tin and copper oxides.
Type B	Archaeological corrosion mechanism in which intergranular corrosion is visible in the inner part of the corrosion layers or just on one side of the sample. Compact and thick layers of different colours are visible on the other side or on the entire surface. Predominant colours are - beside those from the classical corrosion morphology: brownish green, yellow, brown, grey.	Corrosion penetrates inside as a compact and thick layer or inside cracks or preferential areas of the sample - sometimes with a waterfall effect.	Uncommon corrosion features identified as SnO_2*2H_2O and $Sn(OH)_4$ as well as Cuprite (Cu_2O); Cassiterite (SnO_2); Malachite ($Cu_2CO_3(OH)_2$); Azurite ($Cu_3(CO_3)_2(OH)_2$; mixed forms of tin and copper oxides
Type C	Globular shapes corrosion products inside compact layers of different thickness. Predominant colours are - beside those from the classical corrosion morphology: brownish green, yellow, brown, white, grey.	Corrosion penetrates inside the matrix similar to a macro pitting mechanism on entire areas of the sample.	Corrosion features in globular shapes identified as SnO_2*2H_2O and $Sn(OH)_4$; Cuprite (Cu_2O); Cassiterite (SnO_2); Malachite ($Cu_2CO_3(OH)_2$); Azurite ($Cu_3(CO_3)_2(OH)_2$; mixed forms of tin and copper oxides.
Type D	1-1.5 µm wide tunnel shaped structures. The tunnels are never completely straight but bent, dividing and crossing each other, giving the picture of roots or tentacles.	Not following any microstructural features as grain or twinning boundaries or slip bands due to cold deformation. It penetrates directly into the crystal without any regard for the short-circuit of diffusion.	Mixed forms of tin and copper oxides are detected with a predominance of tin-based oxides. Also, SnO_2*2H_2O and $Sn(OH)_4$ are detected.
Type E	Mixtures of previously described corrosion morphologies in which many parameters influenced the corrosion mechanism during relatively long timespans.	Type A, B, C, D	Type A, B, C, D

by a homogeneous microstructure with the presence of an α phase (Figure 3a).

Polygonal grains, typical of recrystallization annealing after deformation are observed, with twinning and slip lines consistent with a last step of cold deformation (Figure 3b). Some residual heterogeneities of the solid solution appeared in some samples, suggesting that the annealing temperature was not high enough to remove residues of the heterogeneity after casting (above 2/3 of the melting temperature of the alloy). Inclusions are made of Fe and Cu sulfides $Cu_{2-x}Fe_xS_2$ and pure Pb islands (given the immiscibility of lead with the Cu-Sn solid solution) (Figure 3b and c). Following equations 1 to 3, the *D* % was calculated. A deformation between 15% and 90% was statistically associated to the microstructure and a frequency plot (not visible) evidences a distribution of the *D* % more pronounced towards higher values (peak at 80 %).

This outcome must however be considered as a function of the grain size and the percentage of Sn inside the solid solution. The grain size varies between 6 µm and 50 µm for M1 (not visible), according to the percentage of Sn in the alloy.

3.2. Corrosion morphology

The corrosion features observed on the range of samples are typologically divided into 5 groups corresponding to alphabetical roman letters (A, B, C, D, E, see Figure 4, Table 1). They are classified according to i) nature and features of the layers (e.g., composition, heterogeneity, thickness), ii) features of penetration (e.g., degree, way). They are resumed in Table 1. The complexity of each corrosion morphology is connected to a specific corrosion mechanism. It is a slow process that follows a logarithmic trend [5] (not considering localized types of corrosion) and the presence of Sn as the major alloying element helps create a mixed Sn and Cu passive oxide, with a protectiveness degree correlated to the amount of Sn in the alloy [17]-[19].

The classical archaeological corrosion (type A or II, Table 1) which has been already mentioned by many authors [7], [33]-[36] is also found this study. From the micro-Raman analysis (Figure 5a) corrosion products as cuprite (Cu_2O), cassiterite (SnO_2), a mixed form of Sn and Cu oxides (spectrum black), malachite ($Cu_2CO_3(OH)_2$-spectrum red), and azurite ($Cu_3(CO_3)_2(OH)_2$ were detected. Impurities as Si, Al are detected by SEM analyses and are responsible for the small shifts of the peaks of some of the compounds [33]. The penetration is intergranular and follows the short-circuits of diffusion [15] where grain boundaries are the anode, and the matrix is the cathode. In those areas a dissolution of Sn is promoted according to the lower standard electrode potential [37] and precipitates in the form of hydroxides and oxides. The formed layer is porous and permeable and thus oxygen can diffuse inward, allowing for the oxidation of Cu. A mixed layer of Cu and Sn oxides is therefore formed (Figure 4a, Figure 5 -black spectrum and Figure 6a - inner layer of corrosion products or IL). Basic Cu carbonates are formed at the outer layer (OL) due to the presence in the soil of CO_2 or carbonate ions in quantities above 200 ppm [38]. A decuprification phenomenon is also observed from the EDS analyses, as well as diffusion processes of minor elements through the corrosion layers [39]-[41]. Figure 6a displays the line-scan profile performed on a representative sample evidencing the interaction of the system alloy/oxide/environment. Calculations on the Sn:Cu atomic ratio along the profile indicate that values are increasing in the IL to a maximum of 2.7, which implies that every 3 atoms of Sn in the oxide are balanced by 1 atom of Cu. As, Pb and Fe enrich the Cu-Sn mixed oxide up to 3-4 times their relative value in the alloy (e.g., from 0.3 wt. % to 1 wt. % for As). This suggests that the diffusion coefficients of those elements are

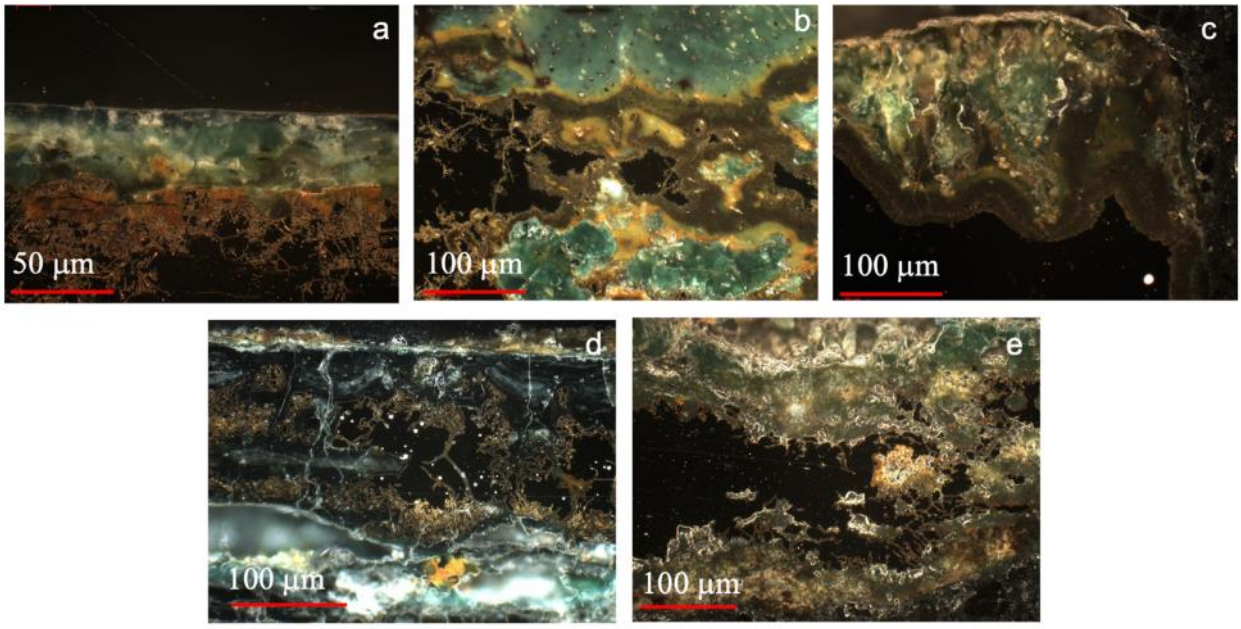

Figure 4. Corrosion morphologies associated to different corrosion mechanisms and defined as: (a) type A; (b) type B; (c) type C; (d) type D; (e) type E.

high enough to migrate inside the corroded layers. Fe shows high concentrations inside the OL (up to more than 10 times the content in the alloy), probably related to its diffusion from the soil. Also Type B corrosion was already detected elsewhere [7] (Figure 4b, Table 1). A compact layer is found at the interface with the metallic matrix. Figure 5b resumes some of the corrosion products found for this peculiar corrosion morphology: an IL of Cu_2O and Sn(OH)4, (spectrum green), followed by SnO_2•$2H_2O$. M*alachite* ($Cu_2CO_3(OH)_2$) or *azurite* ($Cu_3(CO_3)_2(OH)_2$ form in the OL. The Sn oxides, which are thermodynamically stable and have a low solubility limit as doping elements [42], [43], slow down the process. A more severe decuprification phenomenon is detected and values of Sn:Cu from the interface metal/oxide to the edge respectively from 0.2 to 2. However, no enrichment of minor elements was detected in the corrosion layers. Variation of the B type of corrosion, the type C, shows preferential areas of penetration. The corrosion layer is present along cracks sometimes with a "waterfall" effect (Figure 4c, Table 1). Corrosion products are the same as previously mentioned for type B. The Sn:Cu value from the interface metal/oxide to the edge increases as displayed by the line-scans (Figure 6b) and as previously seen, up to 3, which could be possibly connected to a further evolution of the burial context (possibly lack of oxygen) [15]. Pitting can potentially explain the phenomenon, a localized mechanism in which cathodes and anodes are different areas of the sample [14]. However, it is very difficult to detect what triggered the process, either local ruptures of the protective Sn-rich passivation film due to foreign bodies, macro heterogeneities of the film or areas of accumulation of aggressive ions as Cl^- [15].

The type D or "tentacle-like" corrosion [44] does not follow the above-described mechanism but penetrates directly into the crystal without any regard to the short-circuit of diffusion (Figure 4d, Table 1). The morphology shows a tunnel-like structure entering the crystal with apparently irregular directions.

This type of corrosion and its features has led to the hypothesis of a microbial influence in the mechanism and the attribution to Microbiologically Influenced Corrosion (MIC) was proven and discussed more in detail elsewhere [45]-[47]. A

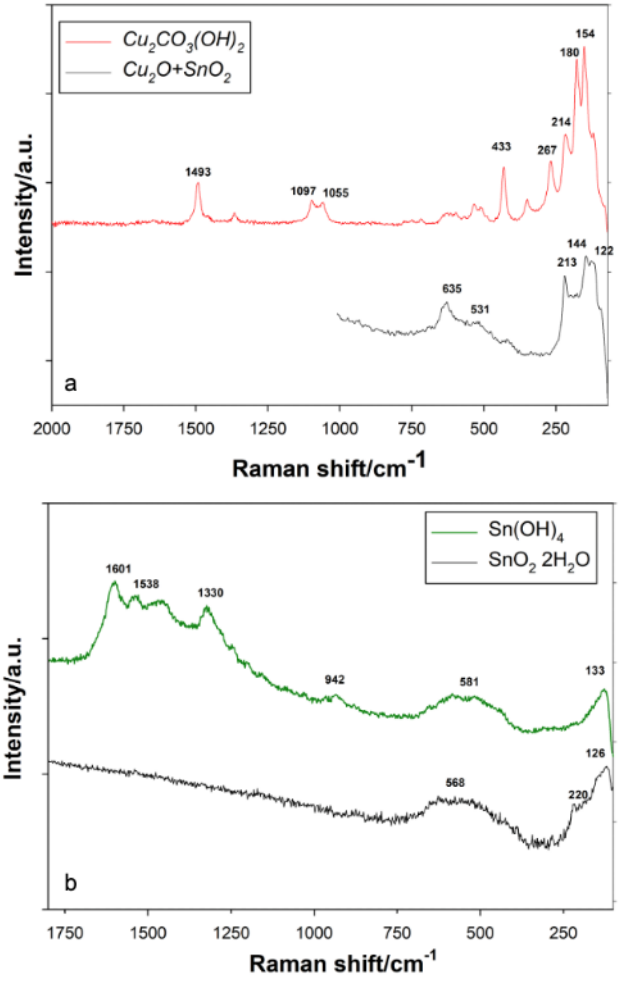

Figure 5. Raman spectra collected with a 632.8 laser on (a) Type A corrosion morphology (b) Type B corrosion morphology; (c) Type D corrosion morphology. Parameters of the analysis: acquisition time: 10 s; number of accumulations: from 1 to 4; power: 25% transmittance. Vibrational bands attribution of: 5a: mixture of Cu_2O and SnO_2; Malachite; 5b: $Sn(OH)_4$; SnO_2*$2H_2O$ with shifts due to the soil

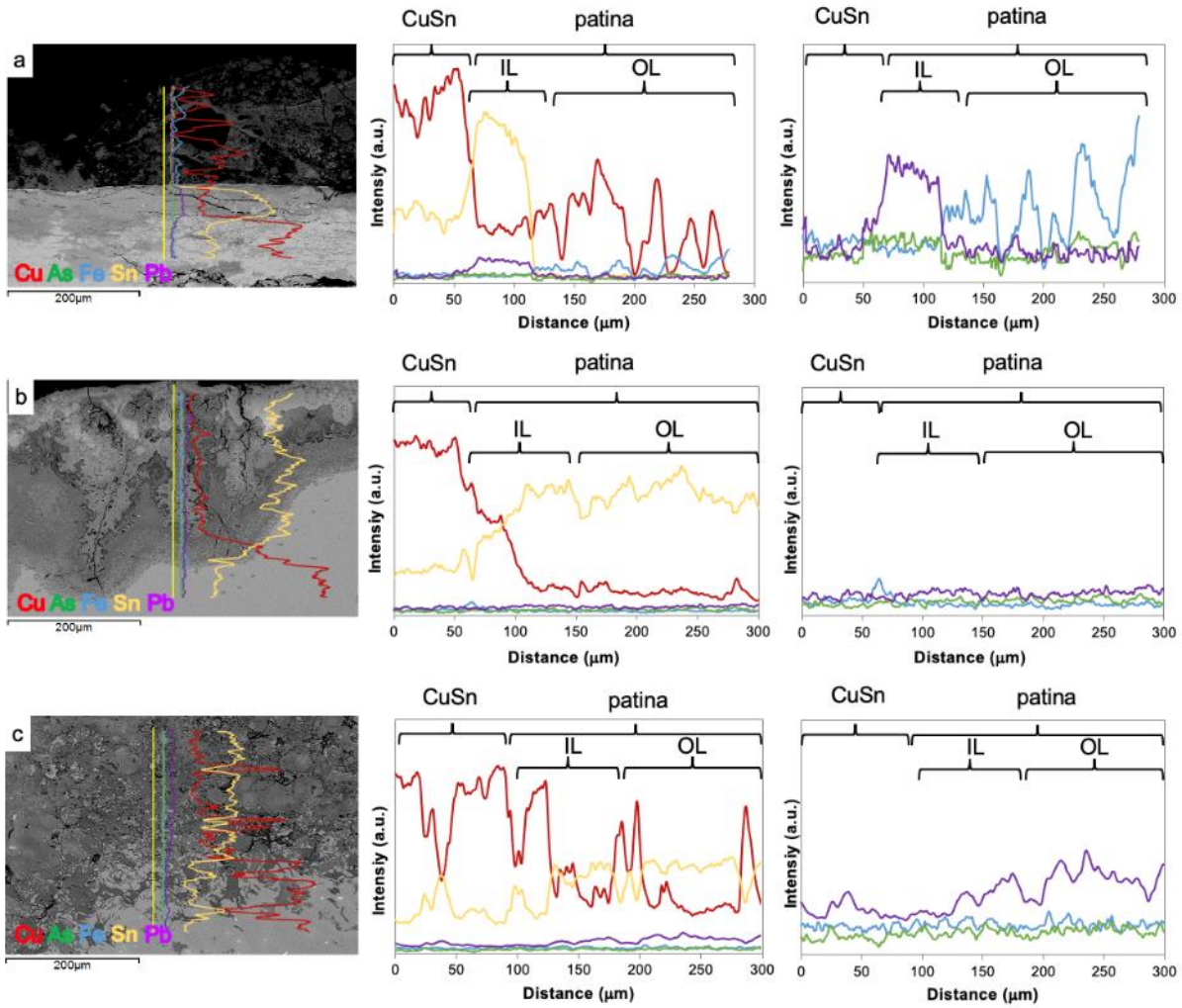

Figure 6. Line-scan profiles of different sites of interest based on the Kα energies of Cu, Sn, Fe, As and Pb of the different morphologies: a) type A; b) type C; c) type D. IL=inner layer of the oxidation patina; OL=outer layer of the oxidation patina.

decuprification process did not occur, as displayed by the line-scan in Figure 6c, since the Kα value of Cu does not decrease linearly but fluctuates along the corrosion layer. Also, higher amounts of Pb are found along the profile towards the OL. Accordingly, the Sn:Cu ratio fluctuates from the metallic interface to the edge with extrema of 0.3 at the interface metal/oxide and a peak of 2 at the IL. This suggests that bacteria promote the formation of Sn products at the IL and a mixed form of Cu and Sn oxides at the OL, influencing the overall corrosion mechanism [47].

When all types of corrosion morphologies are observed on the same artefact with amplitudes which may vary from one area to another, Type E was defined (Figure 4e, Table 1).This type of corrosion was found only on a limited set of samples and is related to changes in the environmental context could lead to the formation of a mixture of the corrosion morphologies. However, the information concerning this corrosion morphology is still under investigation considering the lack of information on the evolution of the environmental conditions.

3.3. Metallurgical parameters on the corrosion process

The correlations between the alloy's microstructural features and the occurrence of typical corrosion morphologies are given by the PCA biplot in Figure 7. As displayed in the graph, correlations between the variables are visible. The distribution of the A type of corrosion referred to the variable Sn is rather

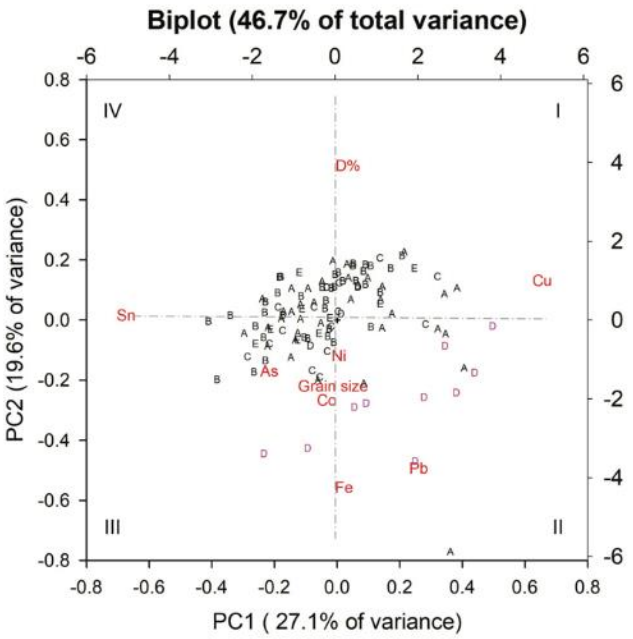

Figure 7. Biplot of the variables influencing the corrosion morphologies considered according to the position of the samples in the newly rotated space. Roman numbers indicate the quadrant.

stochastic. This outcome agrees with other archaeological studies where this type of corrosion was associated to objects in which the Sn content varied enormously, from 5 to 20 in wt. % [5]-[8], [10], [22], as in our case (Figure 8).

Type B and type C corrosion morphologies show a shift in the biplot towards the III quadrant, in the Sn direction. This is consistent with the frequency distribution of the Sn for such morphology (Figure 8), which exhibits a narrow range of composition (from 11 to 15 in wt. % Sn). This could be related to the passivating properties of the element that could shift the corrosion potential towards higher values.

Thus, the composition of the alloy is a rate-controlling factor for the electrochemical corrosion mechanism, as previously stated [17]-[19].

Sn and Cu are not variables that influence Type D morphology since the samples move along a line that connects Cu and Sn (obviously negatively correlated since the increase of one deplete the alloy of the other) as confirmed by the data (Figure 7 and Figure 8). Minor elements (As, Co, Fe, Ni and Pb) do not influence the occurrence of types A, B and C. A trend for corrosion morphology D is discernible from the PCA analysis along a line from the II to the IV quadrant. This morphology is affected by the presence of the minor elements Fe and Pb. This means the higher the concentration of these elements in the alloy (up to a 1.2 wt. % of Pb and 1 wt. % of Fe), the higher the probability to find 'tentacle like' corrosion (MIC) features. It is known that Pb and Fe in sufficient quantity (above 1 %, in our case) modify the corrosion mechanism towards a selective type, culminating with their dissolution [15]. However, it is still not clear how their presence can affect such a morphology since it is influenced by bacterial colonization. We can only infer that their occurrence promotes the microbial attack. We can hypothesize that: i) their dissolution is less harmful for the survival of bacteria compared to Sn and Cu [48], [49]; ii) they can exploit these elements for their metabolism using them as an alternative to carbon as an energy source [50], [51].

The degree of deformation and the grain size affects all types of microstructures to a different extent (Figure 9 and Figure 10). In particular, the degree of deformation seems to positively influence the occurrence of corrosion A, B and C, while it is detrimental for type D. Samples from D type are negatively correlated to *D* % (as they are positioned in the II and III quadrant). This indicates the higher the degree of deformation, the lower the occurrence of type D. Figure 9 describes the degree of deformation according to the morphology observed.

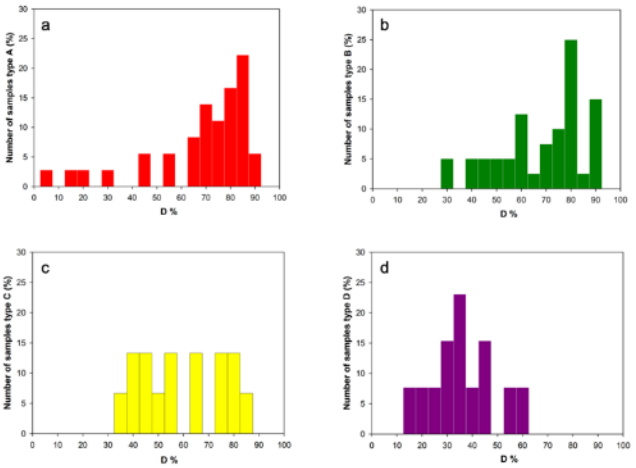

Figure 9. Frequency distribution of the degree of deformation according to the corrosion type detected in the whole range of objects: (a) Type A; (b) Type B; (c) Type C; (d) Type D.

Type D has a frequency distribution centered around 35 %, while for the other morphologies it shifts towards high values (> 65 %). However, the *D* % must be considered as a function of the grain size and all results must be evaluated accordingly. This parameter affects these morphologies differently as suggested by Figure 11 coherently with the outcomes obtained from the *D* %.

A bivariate plot grain size of vs number of samples is displayed in Figure 10. It is evident that the smaller the grain size, the higher the occurrence of corrosion types A, B, and C. The higher the number of polygonal grains, the higher the possibility to find an intergranular penetration since defects and impurities are localized in the areas with higher Gibbs free energy [15]. On the contrary, type D shows an opposite trend. Figure 10d shows a normal distribution of grain size for type D with a peak at around 35-40 µm, which is twice as high compared to the average grain size found for all the samples. This outcome is very interesting but still under study since, to our knowledge, no

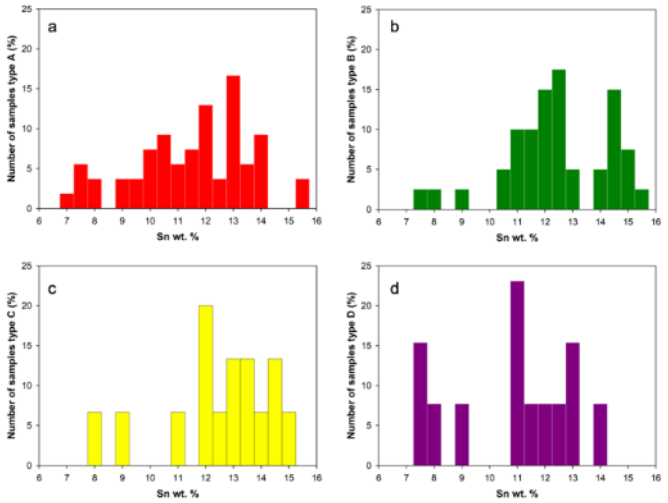

Figure 8. Frequency distribution of the Sn wt % according to the corrosion type detected in the whole range of objects: (a) Type A; (b) Type B; (c) Type C; (d) Type D.

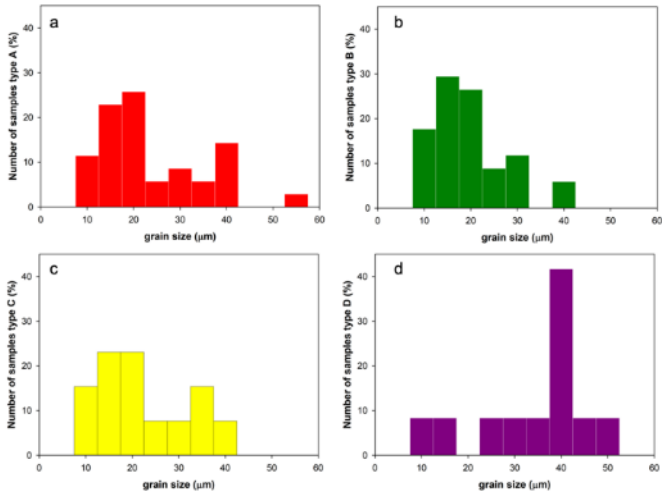

Figure 10. Frequency distribution of the grain size according to the corrosion type detected in the whole range of objects: (a) Type A; (b) Type B; (c) Type C; (d) Type D.

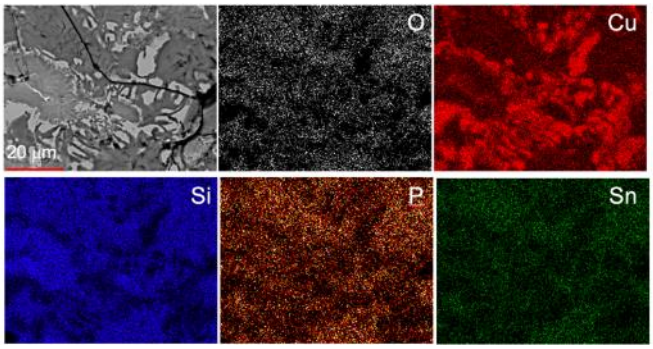

Figure 11. SEM Elemental mapping of Type D corrosion morphology with distribution of the chosen elements along the scanning area.

information is available on the relationship between the grain size, *D* %, and the occurrence of microbial corrosion on Cu-based alloys.

On stainless steels, it seems that the smaller the grain size, the more effective the penetration of the corrosion [52], [53], which is in contradiction with this study. It is indeed difficult to compare the mechanism on a different material with the one found for Cu alloys since the microstructural features are different (e.g., the presence of grain boundaries precipitates). It is only possible to suppose that on a given surface the number of impurities (localized at the grain boundaries) is lower for larger grains, and this could become a key parameter for the survival of the colonies and the occurrence of a bacteria mediated corrosion mechanism. In this perspective, concomitant analyses on both archaeological bronzes with MIC morphology and experimental alloys are needed to better understand the effect of the grain size.

4. CONCLUSION

The main aim of this work is to isolate typical metallurgical parameters that influence the occurrence of specific corrosion morphologies. A categorization of the objects following specific types of composition, microstructure and corrosion was proposed.

The nature of the alloy and the microstructural features act as rate controlling factors for the electrochemical corrosion mechanism. Results show that metallurgical factors do not play a major role in the corrosion morphology of type A, where neither the composition, nor the thermomechanical treatments influence its occurrence. On the other hand, a high correlation of type B and type C to the alloy composition suggests a higher degree of protection due to the Sn tendency to naturally passivate.

The most interesting results come from the type D corrosion morphology (tentacle like or MIC morphology). It is affected by: i) the presence of specific minor elements in the alloy (i.e. Fe and Pb in quantities up to 1%; ii) the presence of microstructure bearing a large grain size (40 µm, twice as high compared to the other morphologies) and a low degree of deformation (peak at 35%). The possible causes for this trend are still doubtful and more research will be carried out in the future to understand this point.

ACKNOWLEDGEMENT

The authors would like to thank the scientific team in charge of the 'project Tintignac', in the person of the major of the city of Naves-en-Corrèze for allowing us to sample the objects; M. Drieux-Daguerre of the Laboratory Materia Viva, Toulouse (FR); B. Armbruster from CNRS-UMR 5608, Toulouse (FR).

REFERENCES

[1] M. Kibblewhite, G. Tóth, T. Hermann, Predicting the preservation of cultural artefacts and buried materials in soil, Sci. Tot. Environm., 529 (2015), pp. 249-263. DOI: 10.1016/j.scitotenv.2015.04.036

[2] J. F. D. Stott, G. John, A. A. Abdullahi, Corrosion in Soils, Reference Module in Materials Science and Materials Engineering, Elsevier, 2018. DOI: 10.1016/B978-0-12-803581-8.10524-7

[3] M. C. Bernard, S. Joiret, Understanding corrosion of ancient metals for the conservation of cultural heritage, Electrochim. Acta, 54(22) (2009), pp. 5199-5205. DOI: 10.1016/j.electacta.2009.01.036 .

[4] F. King, A natural analogue for the long-term corrosion of copper nuclear waste containers—reanalysis of a study of a bronze cannon, Appl. Geochem., 10(4) (1995), pp. 477-487. DOI: 10.1016/0883-2927(95)00019-G .

[5] L. Robbiola, R. Portier, A global approach to the authentication of ancient bronzes based on the characterization of the alloy–patina–environment system, J Cult. Herit., 7(1)1 (2006), pp. 1-12. DOI: 10.1016/j.culher.2005.11.001 .

[6] R. F. Tylecote, The effects of soil conditions on the long-term corrosion of buried tin-bronzes and copper, J. Archaeol. Sci., 6 (1979), pp. 345-368. DOI: 10.1016/0305-4403(79)90018-9 .

[7] L. Robbiola, J.-M. Blengino, C. Fiaud, Morphology and mechanisms of formation of natural patinas on archaeological CuSn alloys, Corros. Sci., 40 (1998), pp. 2083-2111. DOI: 10.1016/S0010-938X(98)00096-1

[8] L. He, J. Liang, X. Zhao, B. Jiang, Corrosion behavior and morphological features of archeological bronze coins from ancient China, Microchem. J, 99 (2) (2011), pp. 203-212. DOI: 10.1016/j.microc.2011.05.009 .

[9] J. Redondo-Marugán, J. Piquero-Cilla, M. T. Doménech-Carbó, B. Ramírez-Barat, W. Al Sekhaneh, S. Capelo, A. Doménech-Carbó, Characterizing archaeological bronze corrosion products intersecting electrochemical impedance measurements with voltammetry of immobilized particles, Electrochim. Acta, 246 (2017), pp. 269-279. DOI: 10.1016/j.electacta.2017.05.190 .

[10] G. M. Ingo, C. Riccucci, C. Giuliani, A. Faustoferri, I. Pierigè, G. Fierro, M. Pascucci, M. Albini, G. Di Carlo, Surface studies of patinas and metallurgical features of uncommon high-tin bronze artefacts from the Italic necropolises of ancient Abruzzo (Central Italy), Appl. Surf. Sci. 470 (2019), pp. 74–83. DOI: 10.1016/j.apsusc.2018.11.115 .

[11] N. Souissi, E. Sidot, L. Bousselmi, E. Triki, L. Robbiola, Corrosion behaviour of Cu–10Sn bronze in aerated NaCl aqueous media – Electrochemical investigation, Corros. Sci. (2007), 49, pp. 3333–3347. DOI: 10.1016/J.CORSCI.2007.01.013

[12] F. Ammeloot, C. Fiaud, E. M. M. Sutter, Characterization of the oxide layers on a Cu-13Sn alloy in a NaCl aqueous solution without and with 0.1 M benzotriazole. Electrochemical and photoelectrochemical contributions, Electrochim. Acta, 44(15) (1999), pp. 2549-2558. DOI: 10.1016/S0013-4686(98)00391-0 .

[13] E. Sidot, N. Souissi, L. Bousselmi, E. Triki, L. Robbiola, Study of the corrosion behaviour of Cu–10Sn bronze in aerated Na2SO4 aqueous solution, Corros. Sci., 48(8) (2006), pp. 2241-2257. DOI: 10.1016/j.corsci.2005.08.020

[14] R. Francis, The corrosion of copper and its alloys: a practical guide for engineers, NACE International, Houston, 2010.

[15] L. L. Shreir, R. A. Jarman, G. T. Burstein, (eds), Corrosion, Butterworth-Heinemann, Oxford, 1963.

[16] R. W. Revie, H. H. Uhlig (eds), Corrosion and corrosion control. An introduction to corrosion science and engineering (4th edition), John Wiley and Sons, Hoboken (NJ), (2008), ISBN: 978-0-471-73279-2

[17] M. J. Hutchison, J. R. Scully, Patina enrichment with SnO2 and its effect on soluble Cu cation release and passivity of high-purity Cu-Sn bronze in artificial perspiration, Electrochim. Acta, 283 (2018), pp. 806-817.
DOI: 10.1016/j.electacta.2018.06.125 .

[18] D. J. Horton, H. Ha, L. L. Foster, H. J. Bindig, J. R. Scully, Tarnishing and Cu ion release in selected copper-base alloys: implications towards antimicrobial functionality, Electrochim. Acta, 169 (2015), pp. 351-366.
DOI: 10.1016/j.electacta.2015.04.001

[19] M. J. Hutchison, P. Zhou, K. Ogle, J. R. Scully, Enhanced electrochemical Cu release from commercial Cu-Sn alloys: fate of the alloying elements in artificial perspiration, Electrochim. Acta, 241(2017), pp. 73-88.
DOI: 10.1016/j.electacta.2017.04.092

[20] E. Sarver, Y. Zhang, M. Edwards, Review of Brass Dezincification Corrosion in Potable Water Systems, Corr. Rev., 28 (3-4) (2010), pp. 155-196.
DOI: CORRREV.2010.28.3-4.155

[21] L. C. Tsao, C. W. Chen Corrosion characterization of Cu–Sn intermetallics in 3.5 wt.% NaCl solution, Corros. Sci. 63 (2012), pp. 393-398.
DOI: 10.1016/j.corsci.2013.11.010

[22] G. M. Ingo, C. Riccucci, G. Guida, M. Pascucci, C. Giuliani, E. Messina, G. Fierro, G. Di Carlo, Micro-chemical investigation of corrosion products naturally grown on archaeological Cu-based artefacts retrieved from the Mediterranean Sea, Appl. Surf. Sci. 470 (2019), pp. 695–706.
DOI: 10.1016/j.apsusc.2018.11.144 .

[23] H. Wei, W. Kockelmann, E. Godfrey, D. A Scott, The metallography and corrosion of an ancient chinese bimetallic bronze sword, J Cult. Herit. 37 (2019), pp. 259–265.
DOI: 10.1016/j.culher.2018.10.004

[24] O. Oudbashi, S. M. Emami, A Note on the Corrosion Morphology of some Middle Elamite Copper Alloy Artefacts from Haft Tappeh, South-West Iran, Stud. Conserv., 55(1) (2010), pp. 20-25.
DOI: 10.1179/sic.2010.55.1.20

[25] D. A. Scott, An Examination of the Patina and Corrosion Morphology of some Roman Bronzes, J Am. Inst. Conserv., 33(1) (1994), pp. 1-23.
DOI: 10.1179/019713694806066419

[26] I. G. Sandu, O. Mircea, V. Vasilache, I. Sandu, Influence of archaeological environment factors in alteration processes of copper alloy artifacts, Microscopy Res. Techn., 75(12) (2012), pp. 1646-1652.
DOI: 10.1002/jemt.22110 .

[27] M. R. Pinasco, M. G. Ienco, P. Piccardo, G. Pellati, E. Stagno, Metallographic approach to the investigation of metallic archaeological objects, Annali di Chimica: J Anal., Environm. Cult. Herit. Chem., 97(7) (2007), pp. 553-574.
DOI: 10.1002/adic.200790037 .

[28] P. Piccardo, M. Pernot, Studio analitico strutturale di alcuni vasi celtici in bronzo, La metallurgia italiana, 11 (1997), pp. 43-52.

[29] M. Mödlinger, P. Piccardo, Manufacture of Eastern European decorative tin-bronze discs from twelfth century BC, Archaeol. Anthropol. Sci. 5 (2013), pp. 299-309.
DOI: 10.1007/s12520-012-0111-6

[30] J. Schindelin, I. Arganda-Carreras, E. Frise, V. Kaynig, M. Longair, T. Pietzsch, S. Preibisch, C. Rueden, S. Saalfeld, B. Schmid, J. Y. Tinevez, D. J. White, V. Hartenstein, K. Eliceiri, P. Tomancak, A. Cardona, Fiji: an open-source platform for biological-image analysis, Nat. Methods 9 (7) (2012), pp. 676-682.
DOI: 10.1038/nmeth.2019 .

[31] Y. Mori, M. Kuroda, N Makino, Nonlinear Principal Component Analysis and Its Applications, Springer, Singapore, 2016.
DOI: 10.1007/978-981-10-0159-8

[32] C. Maniquet, B. Armbruster, M. Pernot, T. Lejars, M. Drieux-Daguerre, L. Espinasse, P. Mora, Aquitania, 27 (2011), pp. 63-150

[33] P. Piccardo, B. Mille, L. Robbiola, Tin and copper oxides in corroded archaeological bronzes in Dillmann, P., Beranger, G., Piccardo, P., Matthiesen. H., Corrosion of Metallic Heritage Artefacts—Investigation, Conservation and Prediction of Long-Term Behaviour, Woodhead, Cambridge, 2007, pp. 239-262
DOI: 10.1533/9781845693015.239

[34] K. Tronner, A.G. Nord, G.C. Borg, Corrosion of archaeological bronze artefacts in acidic soil, Water, Air, Soil Pollut., 85 (1995), pp. 2725-2730.
DOI: 10.1007/BF01186246

[35] G.M. Ingo, T. de Caro, C. Riccucci, E. Angelini, S. Grassini, S. Balbi et al., Large scale investigation of chemical composition, structure and corrosion mechanism of bronze archeological artefacts from Mediterranean basin, Appl Phys A, 83 (2006), pp. 513-520.
DOI: 10.1007/s00339-006-3550-z .

[36] A. Doménech-Carbó, M.T. Doménech-Carbó, I. Martínez-Lázaro, Electrochemical identification of bronze corrosion products in archaeological artefacts. A case study, Microchim Acta, 162 (2008), pp. 351-359.
DOI: 10.1007/s00604-007-0839-3 .

[37] P. Atkins, L. Jones, Chemical Principles: The Quest for Insight (3rd ed.), W.H. Freeman and Company, New York, 2005, ISBN 9781319154196

[38] D. A. Scott, Copper and Bronze in Art: Corrosion, Colorants, and Conservation: Corrosion, Colorants, Conservation, J Paul Getty Museum, New York, 2002.

[39] X. Deng, Q. Zhang, E. Zhou, C. Ji, J. Huang, M. Shao, M. Ding, X. Xu, Morphology transformation of Cu2O sub-microstructures by Sn doping for enhanced photocatalytic properties, J Alloys Comp, 649 (2015), pp. 1124-1129.
DOI: 10.1016/j.jallcom.2015.07.124 .

[40] Y. Du, N. Zhang, C. Wang, Photo-catalytic degradation of trifluralin by SnO2-doped Cu2O crystals, Catalysis Commun., 11 (2010), pp. 670-674.
DOI: 10.1016/j.catcom.2010.01.021 .

[41] N. Budhiraja, Sapna, V. Kumar, M. Tomar, V. Gupta, S. K. Singh, Investigation on Physical Properties of Sn-Modified Cubic Cu2O Nanostructures, J Supercond Nov Magn, 32, 2019, pp. 1671–1679.
DOI: 10.1007/s10948-018-4858-6

[42] C. B. Fitzgerald, M. Venkatesan, A. P. Douvalis, S. Huber, and J. M. D. Coey, SnO2 doped with Mn, Fe or Co: Room temperature dilute magnetic semiconductors, J Appl. Phys., 95 (2004), pp. 7390-7392.
DOI: 10.1063/1.1676026

[43] Z. Junying, Y. Qu, W. Qianghong, Room Temperature Ferromagnetism of Ni-doped SnO2 System, Modern Appl Sci 4(11) (2010)
DOI: 10.5539/mas.v4n11p124

[44] P. Piccardo, M. Mödlinger, G. Ghiara, S. Campodonico, V. Bongiorno, Investigation on a "tentacle-like" corrosion feature on Bronze Age tin-bronze objects, Appl Phys A, 113 (4) (2013), pp. 1039-1047.
DOI: 10.1007/s00339-013-7732-1 .

[45] G. Ghiara, C. Grande, S. Ferrando, P. Piccardo, The influence of Pseudomonas fluorescens on corrosion products of archaeological tin-bronze analogues, JOM, 70(1) (2018), pp. 81-85.
DOI: 10.1007/s11837-017-2674-2

[46] G. Ghiara, L. Repetto, P. Piccardo, The effect of pseudomonas fluorescens on the corrosion morphology of archaeological tin bronze analogues, JOM, 71(2) (2019), pp. 779-783.
DOI: 10.1007/s11837-018-3138-z

[47] G. Ghiara, R. Spotorno, S.P. Trasatti, P. Cristiani, Effect of Pseudomonas fluorescens on the electrochemical behaviour of a single-phase Cu-Sn modern bronze, Corros. Sci., 139 (2018), pp. 227-234.
DOI: 10.1016/j.corsci.2018.05.009 .

[48] B. Little, P. Wagner, F. Mansfeld, An overview of microbiologically influenced corrosion, Electrochim. Acta, 37(12) (1992), 2, pp. 185-2194.
DOI: 10.1016/0013-4686(92)85110-7

[49] B. J. Little, J. S. Lee, Microbiologically Influenced Corrosion, John Wiley and sons, Hoboken, 2007.
[50] D. Enning, J. Garrelfs, Corrosion of Iron by Sulfate-Reducing Bacteria: New Views of an Old Problem, Appl. Environm. Microbiol., 80 (4), (2014), pp. 1226-1236. DOI: 10.1128/AEM.02848-13 .
[51] S. M. Tiquia-Arashiro, Lead absorption mechanisms in bacteria as strategies for lead bioremediation, Appl. Microbiol. Biotechnol., 102(13) (2018), pp. 5437-5444. DOI: 10.1007/s00253-018-8969-6
[52] J. R. Ibars, D. A. Moreno, C. Ranninger, MIC of Stainless Steels: A Technical Review on the Influence of Microstructure, Intern. Biodeter. Biodegrad., 29 (1992), pp. 343-355. DOI: 10.1016/0964-8305(92)90051-O
[53] X. Shi, K. Yang, M. Yan, W. Yan, Y. Shan, Study on Microbiologically Influenced Corrosion Resistance of Stainless Steels With Weld Seams, Front. Mater., (2020). DOI: 10.3389/fmats.2020.00083